Frontiers of Information Technology & Electronic Engineering
www.jzus.zju.edu.cn; engineering.cae.cn; www.springerlink.com
ISSN 2095-9184 (print); ISSN 2095-9230 (online)
E-mail: jzus@zju.edu.cn

Visual recognition of cardiac pathology based on 3D parametric model reconstruction*

Jinxiao XIAO†§1, Yansong LI†§1, Yun TIAN†‡1, Dongrong XU2,3, Penghui LI1, Shifeng ZHAO1, Yunhe PAN3

[1]School of Artificial Intelligence, Beijing Normal University, Beijing 100875, China
[2]Department of Psychiatry, Columbia University & New York State Psychiatric Institute, New York 10032, USA
[3]College of Computer Science and Technology, Zhejiang University, Hangzhou 310027, China
†E-mail: xiaojinxiao@mail.bnu.edu.cn; liyansong@mail.bnu.edu.cn; tianyun@bnu.edu.cn

Received Mar. 16, 2022; Revision accepted July 28, 2022; Crosschecked Aug. 16, 2022

Abstract: Visual recognition of cardiac images is important for cardiac pathology diagnosis and treatment. Due to the limited availability of annotated datasets, traditional methods usually extract features directly from two-dimensional slices of three-dimensional (3D) heart images, followed by pathological classification. This process may not ensure the overall anatomical consistency in 3D heart. A new method for classification of cardiac pathology is therefore proposed based on 3D parametric model reconstruction. First, 3D heart models are reconstructed based on multiple 3D volumes of cardiac imaging data at the end-systole (ES) and end-diastole (ED) phases. Next, based on these reconstructed 3D hearts, 3D parametric models are constructed through the statistical shape model (SSM), and then the heart data are augmented via the variation in shape parameters of one 3D parametric model with visual knowledge constraints. Finally, shape and motion features of 3D heart models across two phases are extracted to classify cardiac pathology. Comprehensive experiments on the automated cardiac diagnosis challenge (ACDC) dataset of the Statistical Atlases and Computational Modelling of the Heart (STACOM) workshop confirm the superior performance and efficiency of this proposed approach.

Key words: 3D visual knowledge; 3D parametric model; Cardiac pathology diagnosis; Data augmentation
https://doi.org/10.1631/FITEE.2200102 **CLC number:** TP391

1 Introduction

Cardiac magnetic resonance imaging (MRI) has become an important tool for diagnosis of cardiac diseases, and computer-aided pathology diagnosis is a critical step in achieving this goal. As the first step of cardiac pathological examination, cardiac segmentation and reconstruction of the imaging data are the keys to obtaining clinical indices, such as ejection fraction (EF), ventricular volume, myocardial mass, and location, size, and volume of stroke. However, annotated datasets are extremely limited in this field. Thus, training automated or machine learning methods for cardiac pathology is a difficult task. Meanwhile, most current machine learning based studies typically focus on segmentation of the left ventricle (LV), right ventricle (RV), and myocardium (MYO) using two-dimensional (2D) slices of three-dimensional (3D) cardiac imaging data to obtain various features (e.g., grayscale statistical features, texture features, and shape features) for pathological classification with the help of different classifiers. There are different criteria for cardiac pathology classification. Statistical Atlases and

§ These authors contributed equally to this work
‡ Corresponding author
* Project supported by the National Natural Science Foundation of China (Nos. 72091511, 62172047, and 61802020)
ORCID: Jinxiao XIAO, https://orcid.org/0000-0002-9666-2943; Yansong LI, https://orcid.org/0000-0002-0749-4344; Yun TIAN, https://orcid.org/0000-0001-5574-2325

Computational Modelling of the Heart (STACOM) 2017 presented a cardiac public dataset, and divided cardiac diseases into five categories: normal (NOR), previous myocardial infarction (MINF), dilated cardiomyopathy (DCM), hypertrophic cardiomyopathy (HCM), and abnormal right ventricle (ARV). Some related works have been done in this field. Isensee et al. (2018) proposed to extract a series of time instances and dynamic features from 2D slices of the cardiac cycle, based on a heavily regularized multilayer perceptron (MLP) and a random forest (RF) classifier that were used for automatic classification of cardiac pathologies. Khened et al. (2018) extracted the features of EF in LV and RV, left and right ventricular volumes at end-systole (ES) and end-diastole (ED) phases, ED myocardial mass, and ES myocardial volume from the segmented 2D slices. Combined with other biological characteristics (height and weight), the extracted features were used as the input to the RF classifier for pathological classification. Wolterink et al. (2018) extracted 14 features from the segmented 2D slices to train a pathology category RF classifier consisting of 1000 decision trees. Cetin et al. (2017) used a semiautomatic segmentation method to manually extract structural contours of the heart, a support vector machine (SVM) as a multifeature classifier, and a few selected image histological features (including shape features, grayscale statistical features, and texture features) as additional inputs. Ammar et al. (2021) proposed an automated pipeline for cardiac segmentation and diagnosis. Traditional 2D image features were extracted via the 2D segmentation of RV, LV, and MYO. Subsequently, the pipeline provided diagnosis of possible heart diseases along with patients' clinical data using an integrated classifier that integrated MLP, RF, and SVM. Some other end-to-end deep learning methods have also been used in cardiac disease classification. A method proposed by Chang and Jung (2020) first reconstructed a 3D surface based on a segmentation result, and obtained uniform 3D pointclouds by randomly sampling the 3D surfaces. Chang and Jung (2020) extracted latent shape features from the cardiac pointclouds based on the PointNet (Charles et al., 2017) and incorporated features such as ventricular volumes and EF for classification of heart disease. Thermos et al. (2021) proposed a framework called "disentangled anatomy arithmetic," in which a generative model learns to combine anatomical factors from different input images to generate new cardiac images, pathology labels, and segmentation masks for augmenting the dataset, thus improving the performance of post-hoc classification and segmentation tasks.

Almost all of these methods used 2D slices of the heart to obtain various features as needed. However, important geometric information characterizing adjacency in the 3D neighborhood was largely lost, putting the overall anatomical consistency of the heart at risk.

In fact, cardiac 3D analysis is essential for the assessment of global and local structural function of the heart (Attar et al., 2019). Shape reconstruction is a bridge between computer vision and computer graphics (Pan, 2021a). Improving the 3D morphological modeling of the heart not only can make the acquired symbolic characteristics more intuitive and reasonable, but also may be helpful for the imagery express of heart knowledge. Pan (2019) proposed the concept of visual knowledge consisting of the prototype and category, which can be used to augment cardiac data and improve the performance of cardiac pathology classification. Inspired by this, 3D cardiac models for different patients with different pathologies at different ages during different phases can be constructed via 3D parametric shape models. Therefore, a large number of models and images can be generated by varying the corresponding parameters to address the problem of limited availability of annotated datasets of cardiac images, and then a cardiac visual knowledge platform covering multiple cardiac pathologies can be constructed.

To address the aforementioned issues, in this study we propose a visual recognition method for cardiac images based on 3D parametric model reconstruction. First, 3D heart models are reconstructed from a number of annotated images, and then based on these reconstructed models, 3D cardiac parametric models of different heart pathologies are constructed through a statistical shape model (SSM), and serve as prototypes of visual knowledge of heart pathology. Second, based on the principal component constraints of SSM, the 3D parametric models are adapted by controlling the shape parameters to match the real pathological features that characterize the same cardiac pathology category. Finally, cardiac disease classification is performed by extracting 3D visual knowledge features of the heart models.

The contributions of this paper are as follows:

1. A 3D cardiac parametric model of different pathological hearts is constructed, and the prototype and category of different cardiac visual knowledge associated with this 3D cardiac parametric model are determined, making it a cardiac visual knowledge model.

2. Based on this visual knowledge model, 3D visual knowledge features (interpretable cardiac shape and motion features) related to cardiac diseases are extracted.

3. Based on the shape parameter constraint of SSM, 3D cardiac data are augmented by sampling in the category with a 3D parametric model.

4. With the augmented data and the 3D shape and motion features of heart models, a reliable classification of cardiac pathology is achieved.

2 Related works

Three-dimensional shape modeling is a powerful tool for quantifying and analyzing cardiac structure and function (Suinesiaputra et al., 2018). In clinical practice, morphological and functional alterations of cardiac ventricles are typical after myocardial lesions due to physiological changes. This self-adaptive or maladaptive process by the body is designed to maintain normal cardiac output (Gjesdal et al., 2011). The International Conference on Medical Image Computing and Computer-Assisted Intervention (MICCAI) has run the STACOM workshop (http://www.cardiacatlas.org/challenges/lv-statistical-shape-modelling-challenge/) for 13 consecutive years since 2010 to discuss issues related to smart cardiac imaging.

Liu and Shi (2009) proposed a computational strategy based on the principle of maximum a posteriori estimation. The method treated the myocardial material model as a random field parameter and used expectation-maximization (EM) to simultaneously estimate motion, deformation, and material parameters, which could produce a sequence of motion states and material parameter estimates for the entire MYO. Gao et al. (2018) first proposed a robust estimation framework with adaptive biomechanical model constraints for the dual $\mathcal{H}_\infty$ criterion, which consisted of two iterative $\mathcal{H}_\infty$ filters, one for kinematic estimation and the other for elasticity estimation, followed by federated estimation of cardiac motion parameters from medical image sequences. Biffi et al. (2019) proposed a conditional variational autoencoder architecture that could effectively reconstruct a 3D high-resolution model of LV by learning a 2D segmentation of the long and short axes of the LV. Chen et al. (2021) proposed a deep learning architecture, called the coined mesh reconstruction network (MR-Net), which enabled accurate 3D mesh reconstruction in real time despite partially missing data and only sparse annotations from 2D contours. These methods focused mainly on how to more accurately reconstruct the 3D mesh structure or parametric model of the heart from the MR image, facilitating the subsequent analysis. In the current study, our approach focuses on constructing the prototype and category of a cardiac pathology, extraction and analysis of 3D visual knowledge features, data augmentation, and pathology classification, based on 3D parametric models.

Geometric registration of a target heart with a template is the key to constructing a 3D SSM of the heart. The point distribution model (PDM) (Cootes et al., 1995) is usually used to describe the shape distribution of the cardiac surface. This description requires that each sample contain the same number of correspondingly sorted vertices and each vertex in the PDM be placed in the same orientation. Since Besl and McKay (1992) proposed the iterative closest point (ICP) registration algorithm, ICP has been widely used for 3D model geometric registration with known initial values of relative position, which iteratively refines the transformation by repeatedly generating corresponding point pairs and minimizing error metrics on the model. The input to the ICP is two pointclouds and an initial transformation that roughly aligns the source pointcloud with the target pointcloud. The output is a transformation matrix of two tightly aligned pointclouds and a transformed copy of the source pointcloud now in the target space. The algorithm has strict requirements for the initial position. If the initial position is not provided correctly, the objective function may easily fall into a local optimal point due to its use of a greedy optimization strategy, which would make it impossible for geometric registration of the 3D heart models.

Bai et al. (2016) conducted a rigid registration by aligning the 3D surface meshes of the images acquired at the ED and ES phases, and then

performed principal component analysis (PCA) (Jolliffe, 2002) on the aligned meshes using the PCA coefficients as a shape feature. The method defined kinematic features based on wall thickness and vertex displacement, and then classified pathology using a support vector regression (SVR) classifier. Parajuli et al. (2016) proposed a cardiology classifier combining an active shape model (ASM) with an SVM. The LV shapes during the ED and ES phases were first aligned with a template LV of the corresponding phases, and the relative difference was maintained. Then, the PCA coefficients of the set of aligned surface points were employed as the feature, and the SVM was employed for pathological classification. Rodero et al. (2021) extracted 3D meshes from 20 normal cardiac computed tomography images, selected 19 3D meshes to create an SSM, and analyzed how specific and local anatomical changes affected different cardiac functional outputs. Bernardino et al. (2020) generated cardiac 3D meshes from the segmentation results of cardiac MRI data and aligned them using a Procrustes analysis (Dryden and Mardia, 1998). Then, the shape variability associated with confounding factors, such as quantitative statistics, was removed, and the most discriminative shape pattern from the coefficients of the classification model was calculated via PCA dimensionality reduction.

These cardiology classification methods focused mostly on studying a single structure or a specific pathology of the heart, but rarely constructed parametric models with multiple sub-structures and pathologies of the heart. Moreover, these methods required precise alignment of the grid data to exclude possible mismatch errors caused by translation and rotation of the shapes. However, due to the irregular structure and shape of the heart, both the Procrustes analysis and the ICP required precise position to initialize the process, and the strict alignment requirement was typically unable to be met. Furthermore, classifier training required a certain amount of evenly labeled data. Unfortunately, the availability of labeled data was usually extremely limited for rare diseases or anatomical samples, even in large-scale medical training datasets. Consequently, the generalizability of the pathological classification model was often weak in such scenarios.

In the last decades, Pan (1996, 2019, 2020, 2021a) proposed new theories concerning visual knowledge representation and cross-knowledge representation, which effectively connected computer vision with computer graphics and provided strong theoretical support for image recognition, particularly in clinical applications for disease diagnosis. Prototype and category are the basic components of visual knowledge. Prototype is the core/mean shape of similar objects. Category is a margin of variation among the core shapes of similar objects, and shapes with the margin belong to the same category. Therefore, in visual knowledge representation of the heart, the average model of different pathological hearts is the prototype, and its category can be determined by principal components with different weight coefficients of 3D SSMs.

3 Proposed methodology

First, a 3D model is reconstructed from each set of labeled 2D images representing different pathologies. Next, based on these reconstructed 3D models, SSM is employed to construct the 3D parametric heart models. The prototype of 3D parametric models is the mean of SSM. The bases of the category are obtained by PCA. Thus, a category is determined via parameter variation of principal components with visual knowledge constraints. Then, the augmentation of heart data can be achieved by random sampling in the category. Finally, shape and motion features of 3D heart models across the two phases are extracted to classify cardiac pathology. The overall flow of the proposed algorithm is shown in Fig. 1.

3.1 3D cardiac parametric model construction

Three-dimensional heart models are reconstructed based on a set of 2D annotation images, which are also referred to as the ground truth of the shape (Fig. 2). In practice, we take advantages of the fast global alignment algorithm (Zhou et al., 2016) and the ICP algorithm (Besl and McKay, 1992) to construct the 3D cardiac parametric model from the reconstructed 3D model data through the SSM. The fast global registration algorithm is first employed to conduct a global and linear registration for two 3D models to be roughly aligned. Then, the ICP algorithm is employed for a fine local registration to obtain the final registration result.

Although the translational and rotational shape

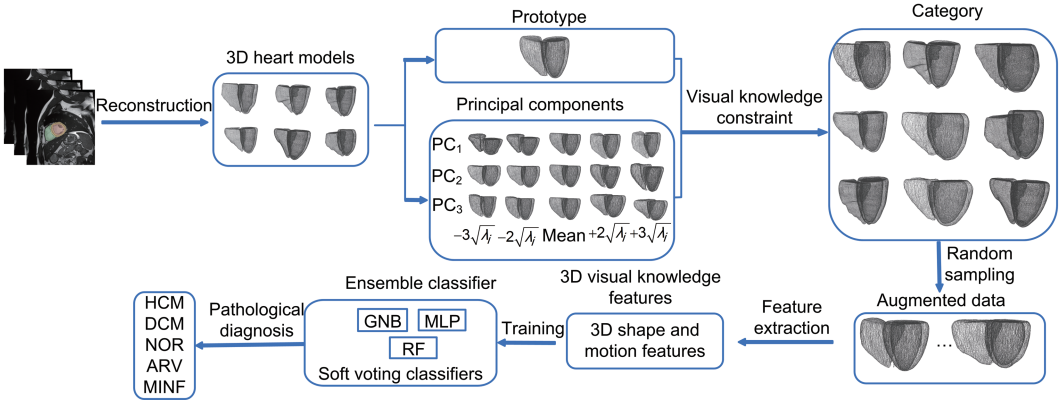

Fig. 1 Overall flow of our proposed algorithm

GNB: Gauss naive Bayes; MLP: multilayer perceptron; RF: random forest; HCM: hypertrophic cardiomyopathy; DCM: dilated cardiomyopathy; NOR: normal; ARV: abnormal right ventricle; MINF: previous myocardial infarction

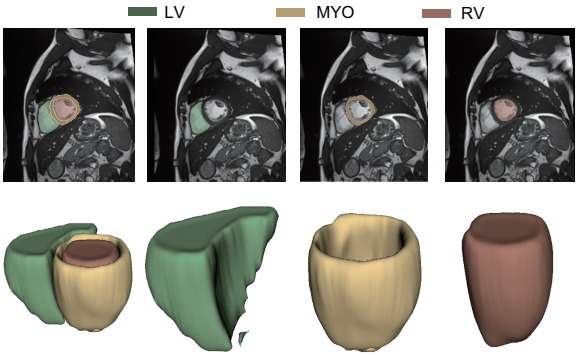

Fig. 2 Schematic of the cardiac tissue and structures as shown in the MRI data

Top row shows the image slices with regions of interest highlighted, and the bottom row shows the reconstructed three-dimensional models of the highlighted structures in the corresponding MRI slices in the top row. LV: left ventricle; MYO: myocardium; RV: right ventricle; MRI: magnetic resonance imaging

variations in the training set can be removed using the fast global alignment and ICP algorithms, the scale variations could not be eliminated. However, the scale between different hearts is an important feature for determining their pathology. As a result, the point (x, y, z) with the minimum Euclidean distance between two models should be found on top of the aligned model as the corresponding point, to ensure the validity of finding the corresponding point. The z-coordinate of each point of all 3D models in the training set needs to be normalized first as

$$\begin{cases} H_{\text{aver}} = \dfrac{1}{n}\sum_{i=1}^{n} H_i, \\ z_j' = \dfrac{z_j}{H_i} H_{\text{aver}}, \end{cases} \tag{1}$$

where H_i is the height of the i^{th} 3D model, which is the distance of the maximum z-coordinate minus the minimum z-coordinate of all points in the model, n is the number of all 3D models, H_{aver} is the average height of all 3D models, z_j is the height of each point in a 3D model before normalization, and z_j' is the height of each point after normalization. After the height is normalized, align the bottom of all 3D models. z_{base} is the height of the points on the bottom plane with zero z-coordinate, and $z_j'' = z_j' - z_{\text{base}}$ is the height of the points of 3D models after height normalization and alignment of the bottom surface.

The correspondence between the template model and all the other models can be established via Eq. (1), and the number of points in each model becomes the same after the above process. Moreover, the points are all placed in the same meaningful position. After that, the height of each model is restored to its original height to ensure the true height information of the model.

After the corresponding points are determined, each 3D model is described by a vector $\boldsymbol{s}$, which contains m coordinates: $\boldsymbol{s}_i = [x_{1i}, y_{1i}, z_{1i}, x_{2i}, y_{2i}, z_{2i}, \ldots, x_{mi}, y_{mi}, z_{mi}]^{\mathrm{T}}$, where i refers to the i^{th} model and m is the number of all points in each model. These vectors form a distribution in the 3D space, and all vectors of model training data are connected to each other. The data matrix $\boldsymbol{S}$ of the whole training set can be expressed as $\boldsymbol{S} = [\boldsymbol{s}_1, \boldsymbol{s}_2, \ldots, \boldsymbol{s}_n]$. The mean shape $\bar{\boldsymbol{s}}$ and the covariance of $\boldsymbol{S}$ are calculated as follows:

$$\begin{cases} \bar{\boldsymbol{s}} = \dfrac{1}{n}\sum_{i=1}^{n} \boldsymbol{s}_i, \\ \boldsymbol{C} = \dfrac{1}{n-1}\sum_{i=1}^{n} (\boldsymbol{s}_i - \bar{\boldsymbol{s}})(\boldsymbol{s}_i - \bar{\boldsymbol{s}})^{\mathrm{T}}. \end{cases} \tag{2}$$

After performing PCA on $\boldsymbol{C}$, we obtain t eigenvectors $\boldsymbol{\Phi} = (\phi_1 | \phi_2 | \cdots | \phi_t)$ and the corresponding eigenvalues λ_i of $\boldsymbol{S}$ in descending order, i.e., $\lambda_i \geq \lambda_{i+1}$. Assuming that all the point vectors of the model follow a multi-dimensional Gaussian probability distribution, we know that any shape inferred by the training set can be approximated from the following linear generative model:

$$\boldsymbol{s} \approx \bar{\boldsymbol{s}} + \boldsymbol{\Phi b}, \tag{3}$$

where $\boldsymbol{b}$ is shape parameter that can be expressed as $\boldsymbol{b} = \boldsymbol{\Phi}^{\mathrm{T}}(\boldsymbol{s} - \bar{\boldsymbol{s}})$ (Frangi et al., 2002). The i^{th} value b_i of parameter $\boldsymbol{b}$ is usually restricted to $|b_i| \leq 3\sqrt{\lambda_i}$ to capture 99.7% of shape variability (Attar et al., 2019).

Each eigenvalue λ_i gives the variance of the training data in the direction of the corresponding eigenvector. As a result, the total variance of the training data is $V = \sum \lambda_i$, and the dimension t of $\boldsymbol{b}$ can be determined by

$$\sum_{i=1}^{t} \lambda_i \geq fV, \tag{4}$$

where f denotes the proportion of the retained variability.

The shape space formed by these vectors contains all possible shape variations for the 3D parametric model simulation, and by optimizing these parameters, different instances of the analyzed shape class can be generated using Eq. (3).

We construct 3D parametric models according to different heart diseases, retaining the pathological characteristics after heart remodeling in different pathologies. At the same time, different substructures of the same pathological heart (LV, RV, and MYO) are constructed separately, and then are combined to obtain the 3D parametric model of the entire heart. Establishing the corresponding 3D parametric model according to different substructures can reduce the complexity of the overall structure while improving the registration accuracy of a single structure.

3.2 Cardiac 3D feature extraction

The American Heart Association (AHA) describes myocardial variations by dividing MYO into 17 segments (Cerqueira et al., 2002). In practice, MYO is usually divided into six segments on all slices along the horizontal short axis (SA) around the base and the middle cavity of the heart for evaluation of cardiac functions.

Some conventional image based clinical indicators, such as ventricular volume and EF, are directly extracted from the 3D model of the heart. Because the 3D model contains the geometric adjacency information of different sub-structures and 3D morphological structure of the heart, the clinical indicators obtained via the model are a better approximation of the real heart volumetric information than those of using 2D slices.

The 3D visual knowledge of the heart, i.e., the left ventricular endocardium and the left ventricular epicardium, can be obtained according to the movement of the heart, as follows:

(1) Variety feature of the MYO: The variety of the MYO is described by the variety of the left ventricular endocardium and the corresponding points on the outer model, which can be used to identify the MINF pathology.

(2) Motion feature of the left ventricular endocardium and epicardium: Varieties in the endocardium and epicardium are described by the variance of the distance in the corresponding points on the endocardium and epicardium of the LV during the ES and ED phases.

The 3D cardiac visual knowledge can be used to describe the shape and motion of the heart, which is reliable and explainable in featuring pathological heart movement. These features are both intuitive and valuable for performing classification tasks.

To calculate 3D visual knowledge features of the left ventricular endocardium and epicardium, we divide the left ventricular endocardium and the adventitia of the 3D heart into 16 layers, and each layer of the MYO is further divided into six segments (Fig. 3). The coordinates of the centroid point corresponding to each layer of the left ventricular endocardium are first obtained via Eq. (5). All points of each layer are at the same height, ensuring that only the x and y of the points in the same layers are calculated:

$$\begin{cases} \bar{x} = \dfrac{1}{n} \sum_{i=1}^{n} x_i, \\ \bar{y} = \dfrac{1}{n} \sum_{i=1}^{n} y_i. \end{cases} \tag{5}$$

We pick a point $\boldsymbol{A}_{i1}(x_{i1}, y_{i1})$ on the endocardium in this layer. Take $\boldsymbol{G}_i(\bar{x}, \bar{y})$ as the center of the circle, and then rotate it clockwise to obtain

the auxiliary point $\boldsymbol{A}'_{ij}(x'_{ij}, y'_{ij})$ $(j = 2, 3, 4, 5, 6)$ as follows:

$$\boldsymbol{T} = \begin{pmatrix} \cos\left(\frac{(j-1)\pi}{3}\right) & \sin\left(\frac{(j-1)\pi}{3}\right) \\ -\sin\left(\frac{(j-1)\pi}{3}\right) & \cos\left(\frac{(j-1)\pi}{3}\right) \end{pmatrix}, \tag{6}$$

$$\begin{cases} \boldsymbol{G}_i\boldsymbol{A}_{i1} = (x_{i1} - \bar{x}, y_{i1} - \bar{y}), \\ \boldsymbol{A}'_{ij}\left(x'_{ij}, y'_{ij}\right) = \boldsymbol{A}_{i1}\left(x_{i1}, y_{i1}\right) + \boldsymbol{G}_i\boldsymbol{A}_{i1}\boldsymbol{T}. \end{cases} \tag{7}$$

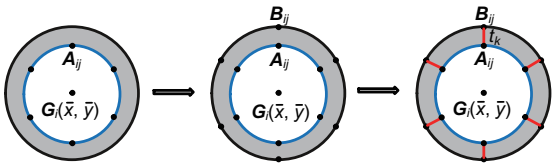

Fig. 3 Corresponding point determination and thickness change of LV

$\boldsymbol{G}_i(\bar{x}, \bar{y})$ is the centroid of the endocardium in the i^{th} layer. $\boldsymbol{A}_{ij}$ is one of the six auxiliary marker sites on the myocardial segments, and $\boldsymbol{B}_{ij}$ is the corresponding point on the epicardium, found using the nearest neighbor method. The gray part and blue outline represent the MYO and the left ventricular endocardium, respectively. The black outline represents the left ventricular epicardium. The red line represents the Euclidean distance t_k between the corresponding points, which measures the thickness of the MYO in this segment. References to color refer to the online version of this figure

Find the nearest neighbor point $\boldsymbol{A}'_{ij}(x'_{ij}, y'_{ij})$ as the representative point of the myocardial segment by the K-nearest neighbor (KNN) algorithm. The nearest neighbor point $\boldsymbol{B}_{ij}(m_{ij}, n_{ij})$ of $\boldsymbol{A}_{ij}$ is found in the point set of the LV. A set of points $(\boldsymbol{A}_{ij}, \boldsymbol{B}_{ij})$ represents this segment of MYO, and the Euclidean distance between the corresponding points is calculated as follows:

$$t_k = \sqrt{(m_{ij} - x_{ij})^2 + (n_{ij} - y_{ij})^2}. \tag{8}$$

Thus, we obtain the thicknesses of 96 different myocardial segments in different layers. Subsequently, the variance s^2 of these distances is calculated to describe the variation in myocardial wall thickness as follows:

$$s^2 = \frac{1}{n-1}\sum_{k=1}^{n}(t_k - \bar{t})^2. \tag{9}$$

Similarly, the variance of the endocardium and adventitia during the ES and ED phases of LV can be obtained to describe the movement of the endocardium and epicardium.

3.3 Data augmentation based on visual knowledge

To facilitate training using a larger amount of data, we augment the cardiac 3D model data based on the visual knowledge and the 3D parametric models as described earlier. The 3D parametric models have been constructed based on different pathological categories, and each of the pathological categories corresponds to a margin of variation among the prototypes. That is, all 3D parametric models from a category belong to the same pathology. As a result, the pathological data can be augmented by random sampling in the margin. In practice, based on the 3D heart prototype, new 3D cardiac data can be obtained by changing the shape parameter elements in vector $\boldsymbol{b}$ within its category according to Eq. (2). However, the resulting cardiac model may not guarantee compliance with the constraints of the cardiac proposition; that is, all sub-structures should maintain anatomical and kinematic consistency. Therefore, it is necessary to impose either the heart proposition constraint in the generating process, or the anatomical knowledge constraint to generate a new heart model.

The visual proposition of the heart has two hierarchies: structural hierarchy and temporal hierarchy. The structural hierarchy is reflected in the structure of the heart which is divided into three parts: LV, RV, and MYO. When the 3D parametric model is deformed to generate data, these three parts should be regarded as a whole, maintaining the uniformity of deformation and moving along the same direction with the same distance. The new data thus generated will still belong to the same heart category, and the new data conform to the structural hierarchy of the heart. The temporal hierarchy is reflected by the fact that the hearts of both the ES and ED phases maintain the correspondence, so that the ES and ED phases of the newly generated cardiac model also correspond to each other.

The cardiac data generated under the constraints of the cardiac visual proposition belong to the same category of the heart and can be regarded as completely new cardiac data. Fig. 1 depicts this specific process of data augmentation.

4 Experiments and analysis

4.1 Automated cardiac diagnostic challenge (ACDC) dataset

The experimental data came from the 2017 MICCAI ACDC (https://www.creatis.insa-lyon.fr/Challenge/acdc/databases.html). It is a dataset specifically designed for the classification of heart diseases. The ACDC dataset consisted of cardiac MR images from 150 subjects, with 100 series of images in the training set and 50 series in the testing set. The 100 series of the training set provided pathology annotations in five categories: NOR, MINF, DCM, HCM, and ARV.

Each category contained a roughly equivalent number of data series in the training and testing sets. The cine MR images were acquired in breath hold with a retrospective or prospective gating using a steady-state free precession (SSFP) sequence along the SA orientation on a 3-Tesla Siemens MRI scanner. A series of SA slices covered LV from the base to the apex, with a slice thickness of 5–8 mm and an interslice gap of 5 or 10 mm. The spatial resolution ranged from 1.37–1.68 mm^2/pixel, and 28–40 images partially or completely covered one cardiac cycle. In addition, each patient's weight, height, and diastolic and systolic phase instants were also collected. Table 1 lists the diagnostic criteria for different pathologies.

In addition, according to the classification rules of cardiology (https://www.creatis.insa-lyon.fr/Challenge/acdc/databasesClassification.html), ambiguous cases should be handled according to the following rules:

1. Patients with HCM should have a left ventricular EF $> 55\%$. Otherwise, patients with a left ventricular EF $< 40\%$ and a local increase in myocardial thickness (as an adaptation of MYO to the disease) must be classified as patients with MINF.

2. Patients with an abnormally high left ventricular diastolic volume, low left ventricular EF, and only several myocardial segments with abnormal contraction must be classified as patients with MINF. Indeed, the increase in the volume of LV is an adaptation of the LV due to a myocardial infarction.

3. Patients with dilated LV and RV (with or without abnormal function of the RV) must be classified as patients with DCM. Indeed, DCM of LV could have an impact on RV.

4. Patients with borderline values should not be included in one particular class. For example, a patient with EF of RV $> 45\%$ is considered normal, but a patient with EF of RV between 40% and 45% cannot be classified as a patient with an ARV.

As discussed later in this paper, these ambiguities do have an impact on the classification results and are the biggest challenge in the classification task.

4.2 Prototype of different pathological hearts and their category construction

To construct the prototype, as well as the category of the heart, a 3D model is first reconstructed using the label maps of the ED and ES instances in the training set of the ACDC dataset. Three-dimensional models of LV, RV, and MYO of each patient's heart snapshotted during the ED and ES phases are separately reconstructed, as described in Section 3.1. Then, the 3D model of one patient in each pathology type is randomly selected as the template model, and the fast global registration algorithm (Zhou et al., 2016) and the ICP algorithm (Besl and McKay, 1992) are used to register the 3D model data of the corresponding heart structure with the same pathology in the training set to the template model to eliminate the shape differences due to translation and rotation in the training set. Then, all the 3D models in the same template space are in

Table 1 Diagnostic criteria for different pathologies

Pathological type	Diagnostic criteria
ARV	The right ventricular volume is > 110 mL/m^2 or the right ventricular EF is $< 40\%$
MINF	The left ventricular EF is $< 40\%$ and the contraction of multiple myocardial segments is abnormal
DCM	During ED, the left ventricular volume is > 100 mL/m^2, and the left ventricular EF is $< 40\%$
HCM	The left ventricular mass is > 110 g/m^2, the thickness of several myocardial segments is > 15 mm during ED, and the EF is normal

ARV: abnormal right ventricle; MINF: previous myocardial infarction; DCM: dilated cardiomyopathy; HCM: hypertrophic cardiomyopathy; EF: ejection fraction; ED: end-diastole

place to obtain the corresponding points.

Fig. 4 shows the prototypes of hearts with different pathologies. It is clear that the prototypes of different pathologies differ greatly in the shape of their corresponding lesion structures; for example, the sizes of the LV of DCM and NOR are different in the ED phase, the sizes of the RV of ARV and NOR are different in the ED phase, and the sizes of the LV of HCM and NOR are different in the ES phase. In addition, if the prototype is thus constructed following the procedure of calculating the 3D parametric model, the obtained shape model would hide the true characteristics that may identify MINF pathology.

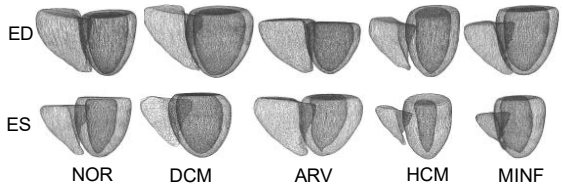

Fig. 4 Prototype demonstration of normal hearts and different pathologies

Top row shows the hearts in the end-diastole (ED) phase, and the bottom row shows the hearts in the end-systole (ES) phase. NOR: normal; DCM: dilated cardiomyopathy; ARV: abnormal right ventricle; HCM: hypertrophic cardiomyopathy; MINF: previous myocardial infarction

To determine the pathology category, we characterize the sub-structure of each heart using PCA, with the principal components sorted in descending order of the eigenvalues. Seventeen principal components are calculated to cover $> 99.7\%$ of the changing patterns via inequality (4).

To visually show the effects of different principal components on the heart structure, we use the first three principal components PC_1, PC_2, and PC_3 to create a visual model of the whole heart structure. PC_i denotes the i^{th} principal component, and the corresponding eigenvalues vary between $-3\sqrt{\lambda_i}$ and $+3\sqrt{\lambda_i}$. Figs. 5 and 6 show the prototype and the category changes of NOR and DCM hearts, respectively.

Figs. 5 and 6 show the shape changes of the 3D heart model associated with PC_1, PC_2, and PC_3. It can be seen that different components control different changes in the heart. PC_1 is related to the height and width of the overall heart structure. PC_2 is related to sizing the lower part of the overall heart structure. PC_3 is related to the enlargement and shrinkage of the overall heart structure in the horizontal direction. The changes decrease gradually with decreasing eigenvalues.

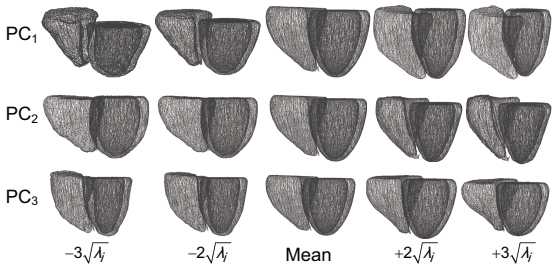

Fig. 5 Prototype of the normal (NOR) pathology and instances of the NOR category

The prototype of the NOR is generated using 18 aligned 3D NOR models. The instance is generated by changing a single shape parameter component (b_{ij}) and fixing all the other parameters at a zero standard deviation from the prototype. This model consists of 2843 left ventricular nodes, 4799 myocardial nodes, and 4857 right ventricular nodes

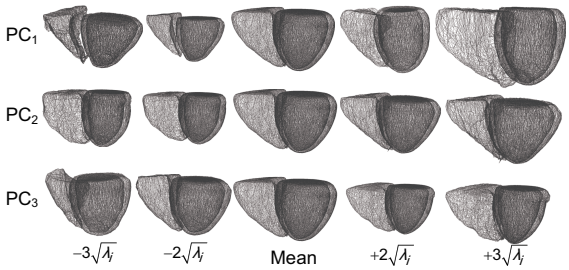

Fig. 6 Prototype of the DCM pathology and instances of the DCM category

The prototype of the dilated cardiomyopathy (DCM) is generated using 18 aligned 3D DCM models. The instance is generated by changing a single shape parameter component (b_{ij}) and fixing all the other parameters at a zero standard deviation from the prototype. The model consists of 4402 left ventricular nodes, 6968 myocardial nodes, and 2787 right ventricular nodes

4.3 Comparison of the classification of 3D visual knowledge features and conventional image based features

For the next pathological diagnosis, we extract 16 features from the 3D model data. Twelve features with seven types are conventional image based features, and four are 3D visual knowledge features including the myocardial wall thickness and the myocardial motion features snapshotted during the ES and ED phases, as shown in Tables 2 and 3.

Results of disease classification based on conventional image based features alone versus conventional image based features with 3D visual knowledge features using different machine learning classifiers are compared in Table 4. Our 3D visual knowledge

features can enhance the effect of disease diagnosis to a certain extent. Compared to Gauss naive Bayes (GNB), RF, and MLP, the ensemble classifier, a strategic combination of GNB, RF, and MLP, performs the best. We therefore choose it for the subsequent classification experiments. Fig. 7 shows the confusion matrices of conventional image based features and conventional image based features with 3D visual knowledge features when the ensemble classifier is used. It can be seen that our 3D visual knowledge features not only classify the NOR, HCM, and ARV correctly in the testing set on the ACDC dataset, but also enhance the accuracy of identifying the DCM and MINF pathologies, which are often difficult to distinguish. In brief, incorporating 3D visual knowledge can improve the MINF and DCM classification accuracy.

Table 2 Seven types of conventional image based features

Feature	LV	RV	MYO
Volume at ED	√	√	√
Volume at ES	√	√	√
EF	√	√	
ES[vol(LV)/vol(RV)]	√	√	
ED[vol(LV)/vol(RV)]	√	√	
ED[vol(MYO)/vol(LV)]	√		√
ES[vol(MYO)/vol(LV)]	√		√

ED: end-diastole; ES: end-systole; EF: ejection fraction; LV: left ventricle; RV: right ventricle; MYO: myocardium

Table 3 Four types of 3D visual knowledge features

Feature	LV	RV	MYO
Variance of myocardial wall at ED			√
Variance of myocardial wall at ES			√
Variance of LV at ED and ES			√
Variance of myocardial at ED and ES			√

ED: end-diastole; ES: end-systole; LV: left ventricle; RV: right ventricle; MYO: myocardium

4.4 Pathological data augmentation

The classification results in Fig. 7b in Section 4.3 demonstrate that the two misclassified categories are the MINF and DCM, due to the strong similarity between the MINF and DCM categories. Hearts classified as DCM lack global myocardial

Table 4 Disease classification results using different machine learning classifiers on the ACDC testing set (50 cases)

Method	Accuracy (%)	
	Alone	Combination
GNB	84	**92**
MLP	**88**	86
RF	86	**88**
Ensemble	84	**94**

Alone means conventional image based features alone, and combination means the combination of conventional image based features with 3D visual knowledge features. ACDC: automated cardiac diagnostic challenge; GNB: Gauss naive Bayes; MLP: multilayer perceptron; RF: random forest. Best results are in bold

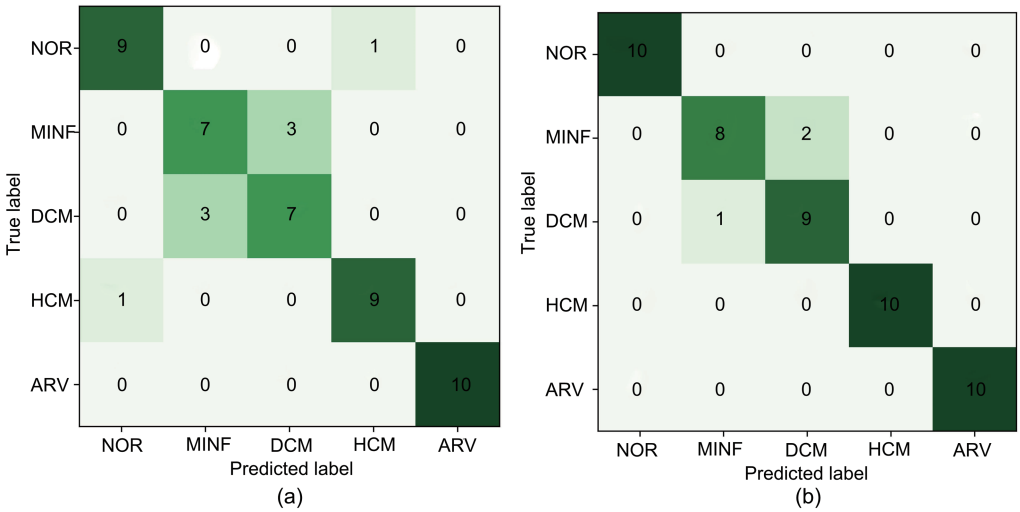

Fig. 7 Confusion matrices of classification results on the ACDC testing set (50 cases) using the ensemble classifier: (a) results based on conventional image based features; (b) results based on the combination of conventional image based features and 3D visual knowledge features

Rows correspond to the predicted category and columns correspond to the target category. ACDC: automated cardiac diagnostic challenge; NOR: normal; MINF: previous myocardial infarction; DCM: dilated cardiomyopathy; HCM: hypertrophic cardiomyopathy; ARV: abnormal right ventricle

contraction, whereas those classified as MINF are limited to a few myocardial segments. The feature of abnormal shrinkage mentioned in the MINF category is actually rather vague. In addition, left ventricular EF is lower in both the MINF and DCM patients. In certain cases, myocardial infarction may cause LV dilation, which makes cardiac classification a challenging task. We should take measures of data augmentation to help improve the efficiency of the classifiers when dealing with these two types of pathologies.

Data augmentation is implemented using our method as presented in Section 3.3. There are many aspects in a heart model that can be regarded as stochastic. Any of these can be randomized without affecting our perception of the model, as long as they follow a reasonable distribution (Karras et al., 2019). New cardiac data can be obtained from the training set by changing the features of the heart SSM (Van Dijck et al., 2018). The first seven features of the cardiac shape extracted by PCA in Section 4.2 are used mainly in the generating process, because the first seven features already cover 85% of the shape features of the cardiac model, and the remaining features are considered to be nuance caused by local details.

We use the 3D cardiac parametric model to fit real-world heart model data to explore the range of parameter $\boldsymbol{b}$. The results show that the first three elements ($i = 1, 2, 3$) of parameter $\boldsymbol{b}$ for the real-world heart are within $\left[-2\sqrt{\lambda_i}, +2\sqrt{\lambda_i}\right]$ and the last four values ($i = 4, 5, 6, 7$) are within $\left[-\sqrt{\lambda_i}, +\sqrt{\lambda_i}\right]$. We therefore believe that the first three features have a greater impact on the shape of the heart model, because these three features concern important geometry factors of the heart, for example, the height and the cross-sectional dimensions, whereas the remaining four features concern some local features of the heart.

Most generating work has employed a multivariate standard normal distribution $\mathcal{N}(0, I)$ or uniform distribution $\mathcal{U}(-1, 1)$ as the prior for $\boldsymbol{z}$ (Brock et al., 2019). In this study, a seven-dimensional noise $\boldsymbol{z}$ is sampled from $\mathcal{N}(0, I)$. For the sampled noise, only the first three dimensional values in $[-2, 2]$ and the last four dimensional values in $[-1, 1]$ are retained, to meet the requirements of the generated features mentioned earlier. To ensure that the generated models are consistent with the original cardiac models in terms of cardiac anatomy and motion, we use the same $\boldsymbol{z}$ to generate three sub-structures (LV, RV, and MYO) of the same heart at different phases (ED/ES). For any sub-structure k, its corresponding parameter $\boldsymbol{b}_k$ is calculated using $\boldsymbol{z}$ and the eigenvalues $\lambda_{k,j}$:

$$\boldsymbol{b}_k = \left[\lambda_{k,1}, \lambda_{k,2}, \cdots \lambda_{k,7}\right]^{\mathrm{T}} \boldsymbol{z}, \tag{10}$$

and the new model $\boldsymbol{s}_k$ can be calculated according to Eq. (3).

The prototype of the MINF pathology could be confused with those of the other types of pathology. Thus, it cannot be used to generate new MINF data by changing the shape parameter elements in vector $\boldsymbol{b}$ within its category according to Eq. (3). Hence, we choose to generate new DCM data to augment the dataset and improve the generalizability of the pathology classification model. In this study, a total of 20 new DCM datasets are generated and added to the training set for testing diagnosis on the testing set using an ensemble classifier. Table 5 lists the noise $\boldsymbol{z}$ and parameter $\boldsymbol{b}$ for a generated DCM model, where the first three $\boldsymbol{b}_k$ ($k = 1, 2, 3$) and the last three $\boldsymbol{b}_k$ ($k = 4, 5, 6$) are the parameters of the LV, RV, and MYO structures in the ED and ES phases, respectively. Parts of the augmentation data are shown in Fig. 8.

Only one case of MINF and one case of DCM are not classified correctly in the final result (Fig. 9), and the two cases have a high degree of similarity. For the MINF case, its left ventricular volume may usually have an expansion, which indirectly leads to the occurrence of DCM. Therefore, the reason why these two cases are not correctly classified may be the similarity of the characteristics of MINF and DCM.

When a number of conventional feature based machine learning methods (Cetin et al., 2017; Isensee et al., 2018; Khened et al., 2018; Wolterink et al., 2018; Zheng et al., 2019; Ammar et al., 2021) and

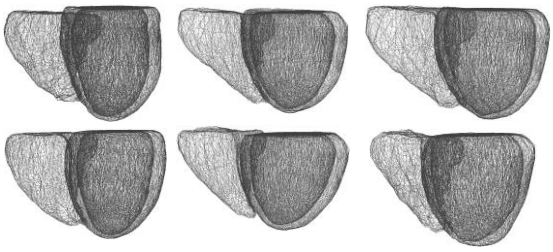

Fig. 8 New dilated cardiomyopathy (DCM) data display with different parameters $\boldsymbol{b}$

Table 5 Noise z and the corresponding parameter b of a generated dilated cardiomyopathy (DCM)

Dimension	Noise z	b_1	b_2	b_3	b_4	b_5	b_6
1	1.785 553 21	393.3479	509.718	423.1248	362.1643	490.8532	378.251
2	1.583 254 10	198.2308	226.3166	205.2633	209.0502	187.0769	202.1402
3	0.760 217 93	82.101 73	90.598 82	75.765 59	66.888 94	76.771 07	71.243 02
4	0.593 141 97	48.418 12	49.673	49.100 32	51.434 54	54.879 08	45.1232
5	−0.485 891 56	−29.3559	−32.8991	−35.0705	−29.3251	−32.5167	−27.7675
6	−0.022 931 55	−1.321 09	−1.402 52	−1.507 11	−1.167 21	−1.415 05	−1.252 35
7	0.058 637 42	3.155 731	3.408 775	3.622 214	2.670 804	3.323 664	2.699 738

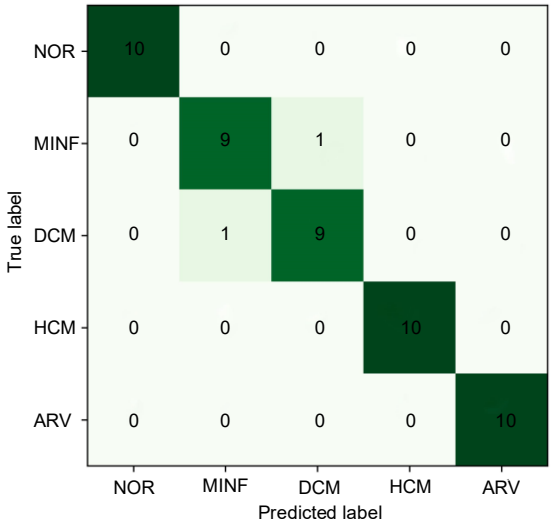

Fig. 9 Confusion matrix of the classification results of the ACDC testing set (50 cases) using the ensemble classifier after adding 20 cases of the DCM data to the training set

Rows correspond to the predicted class and columns correspond to the target class. ACDC: automated cardiac diagnostic challenge; NOR: normal; MINF: previous myocardial infarction; DCM: dilated cardiomyopathy; HCM: hypertrophic cardiomyopathy; ARV: abnormal right ventricle

some end-to-end deep learning methods (Chang and Jung, 2020; Thermos et al., 2021) were tested on the ACDC testing set (Table 6), the classification accuracy of our method was 96%, which is comparable to that of the two-stage classification method proposed by Khened et al. (2018). It is worth noting that our method has performed the classification task only once. Although our method uses fewer features and a single-stage classification process, it achieves better classification results, which proves the effectiveness of using 3D visual knowledge features and the data augmentation method as proposed in this study.

Deep learning based methods are often less satisfactory because of the limitations of the ACDC dataset size. Chang and Jung (2020) used pointcloud features and conventional image based features to achieve a classification accuracy of 94%, and the accuracy of using pointcloud features alone was 88%. Thermos et al. (2021) achieved a classification accuracy of 91% by synthesizing new data. This showed the effectiveness of conventional image based features and the relative inapplicability of deep learning methods in small datasets like ACDC. Moreover, the results of deep learning based methods are usually impossible to explain. Therefore, the "diagnostic black box" could not be integrated as is in a clinical practice (Bernard et al., 2018). In addition to the pathological prediction, a medical report must always record the pathology reasons why a patient is diagnosed, for example, EF, volume, and mass, and/or other cardiac parameters. In contrast, the features extracted and the classification made in this study are all based on cardiac vision knowledge. Our efforts and results demonstrate that the visual knowledge features extracted in this study are clinically relevant and are therefore valuable for clinical cardiac applications.

Table 6 Classification accuracy of different models on the automated cardiac diagnostic challenge (ACDC) testing set (50 cases)

Method	Accuracy (%)
Isensee et al. (2018)'s	92
Wolterink et al. (2018)'s	86
Cetin et al. (2017)'s	88
Zheng et al. (2019)'s	94
Khened et al. (2018)'s	96
Ammar et al. (2021)'s	92
Chang and Jung (2020)'s	94
Thermos et al. (2021)'s	91
Ours	96

5 Conclusions

We propose a method for visual recognition of cardiac pathology based on 3D parametric model reconstruction. Three-dimensional heart model data

are first reconstructed from annotated cardiac image data, and then based on these reconstructed 3D models, SSM is employed to construct 3D parametric models of hearts with different pathologies. Combining the visual knowledge of cardiac pathologies, each of the pathological categories is determined through the parameter variation of principal components with visual knowledge constraints. Then, the cardiac data are augmented by random sampling in the category. Conventional image based features and 3D visual knowledge features of the 3D model of the heart are subsequently extracted to classify cardiac pathology. Comprehensive experiments are done on the ACDC dataset, and the results illustrate good performance of the proposed approach. Data augmentation based on 3D visual knowledge constraints has achieved especially positive results in the diagnosis of some specific pathologies. This can effectively solve the problem of insufficient samples, and has a good universal applicability in medical image processing. In the future work, we shall focus on the study of a 3D parametric model of the cardiac system, the construction of 3D visual knowledge of the cardiac system, and the expression of multiple pieces of knowledge of the cardiac system. We shall also try combining visual semantic primitives and semantic graph networks to investigate the interpretability of disease diagnosis.

Contributors

Yun TIAN and Yunhe PAN designed the research. Jinxiao XIAO and Yansong LI conducted the experiments and drafted the paper. Penghui LI and Shifeng ZHAO helped organize the paper. Dongrong XU revised and finalized the paper.

Compliance with ethics guidelines

Jinxiao XIAO, Yansong LI, Yun TIAN, Dongrong XU, Penghui LI, Shifeng ZHAO, and Yunhe PAN declare that they have no conflict of interest.

References

Ammar A, Bouattane O, Youssfi M, 2021. Automatic cardiac cine MRI segmentation and heart disease classification. *Comput Med Imag Graph*, 88:101864. https://doi.org/10.1016/j.compmedimag.2021.101864

Attar R, Pereañez M, Bowles C, et al., 2019. 3D cardiac shape prediction with deep neural networks: simultaneous use of images and patient metadata. Proc 22nd Int Conf on Medical Image Computing and Computer-Assisted Intervention, p.586-594. https://doi.org/10.1007/978-3-030-32245-8_65

Bai WJ, Oktay O, Rueckert D, 2016. Classification of myocardial infarcted patients by combining shape and motion features. Proc 6th Int Workshop on Statistical Atlases and Computational Models of the Heart, p.140-145. https://doi.org/10.1007/978-3-319-28712-6_15

Bernard O, Lalande A, Zotti C, et al., 2018. Deep learning techniques for automatic MRI cardiac multi-structures segmentation and diagnosis: is the problem solved? *IEEE Trans Med Imag*, 37(11):2514-2525. https://doi.org/10.1109/TMI.2018.2837502

Bernardino G, Benkarim O, Sanz-de la Garza M, et al., 2020. Handling confounding variables in statistical shape analysis-application to cardiac remodelling. *Med Image Anal*, 65:101792. https://doi.org/10.1016/j.media.2020.101792

Besl PJ, McKay ND, 1992. A method for registration of 3-D shapes. *IEEE Trans Patt Anal Mach Intell*, 14(2):239-256. https://doi.org/10.1109/34.121791

Biffi C, Cerrolaza JJ, Tarroni G, et al., 2019. 3D high-resolution cardiac segmentation reconstruction from 2D views using conditional variational autoencoders. Proc IEEE 16th Int Symp on Biomedical Imaging, p.1643-1646. https://doi.org/10.1109/ISBI.2019.8759328

Brock A, Donahue J, Simonyan K, 2019. Large scale GAN training for high fidelity natural image synthesis. https://arxiv.org/abs/1809.11096

Cerqueira MD, Weissman NJ, Dilsizian V, et al., 2002. Standardized myocardial segmentation and nomenclature for tomographic imaging of the heart—a statement for healthcare professionals from the Cardiac Imaging Committee of the Council on Clinical Cardiology of the American Heart Association. *Circulation*, 105(4):539-542. https://doi.org/10.1161/hc0402.102975

Cetin I, Sanroma G, Petersen SE, et al., 2017. A radiomics approach to computer-aided diagnosis with cardiac cine-MRI. Proc 8th Int Workshop on Statistical Atlases and Computational Models of the Heart, p.82-90. https://doi.org/10.1007/978-3-319-75541-0_9

Chang YK, Jung C, 2020. Automatic cardiac MRI segmentation and permutation-invariant pathology classification using deep neural networks and point clouds. *Neurocomputing*, 418:270-279. https://doi.org/10.1016/j.neucom.2020.08.030

Charles RQ, Su H, Mo KC, et al., 2017. PointNet: deep learning on point sets for 3D classification and segmentation. Proc IEEE Conf on Computer Vision and Pattern Recognition, p.77-85. https://doi.org/10.1109/CVPR.2017.16

Chen X, Ravikumar N, Xia Y, et al., 2021. Shape registration with learned deformations for 3D shape reconstruction from sparse and incomplete point clouds. *Med Imag Anal*, 74:102228. https://doi.org/10.1016/j.media.2021.102228

Cootes TF, Taylor CJ, Cooper DH, et al., 1995. Active shape models—their training and application. *Comput Vis Imag Underst*, 61(1):38-59. https://doi.org/10.1006/cviu.1995.1004

Dryden IL, Mardia KV, 1998. Statistical Shape Analysis. John Wiley & Sons, London, UK, p.663-669.

Frangi AF, Rueckert D, Schnabel JA, et al., 2002. Automatic construction of multiple-object three-dimensional statistical shape models: application to cardiac modeling. *IEEE Trans Med Imag*, 21(9):1151-1166. https://doi.org/10.1109/TMI.2002.804426

Gao ZF, Zhang HY, Wang DF, et al., 2018. Robust recovery of myocardial kinematics using dual $\mathcal{H}_\infty$ criteria. *Multim Tools Appl*, 77(17):23043-23071. https://doi.org/10.1007/s11042-017-5395-1

Gjesdal O, Bluemke DA, Lima JA, 2011. Cardiac remodeling at the population level—risk factors, screening, and outcomes. *Nat Rev Cardiol*, 8(12):673-685. https://doi.org/10.1038/nrcardio.2011.154

Isensee F, Jaeger PF, Full PM, et al., 2018. Automatic cardiac disease assessment on cine-MRI via time-series segmentation and domain specific features. Proc 8$^{\text{th}}$ Int Workshop on Statistical Atlases and Computational Models of the Heart, p.120-129. https://doi.org/10.1007/978-3-319-75541-0_13

Jolliffe IT, 2002. Principal component analysis. *J Mark Res*, 87(4):513.

Karras T, Laine S, Aila T, 2019. A style-based generator architecture for generative adversarial networks. Proc IEEE/CVF Conf on Computer Vision and Pattern Recognition, p.4396-4405. https://doi.org/10.1109/CVPR.2019.00453

Khened M, Alex V, Krishnamurthi G, 2018. Densely connected fully convolutional network for short-axis cardiac cine MR image segmentation and heart diagnosis using random forest. Proc 8$^{\text{th}}$ Int Workshop on Statistical Atlases and Computational Models of the Heart, p.140-151. https://doi.org/10.1007/978-3-319-75541-0_15

Liu HF, Shi PC, 2009. Maximum a posteriori strategy for the simultaneous motion and material property estimation of the heart. *IEEE Trans Biomed Eng*, 56(2):378-389. https://doi.org/10.1109/TBME.2008.2006012

Pan YH, 1996. The synthesis reasoning. *Patt Recogn Artif Intell*, 9(3):201-208 (in Chinese).

Pan YH, 2019. On visual knowledge. *Front Inform Technol Electron Eng*, 20(8):1021-1025. https://doi.org/10.1631/FITEE.1910001

Pan YH, 2020. Multiple knowledge representation of artificial intelligence. *Engineering*, 6(3):216-217. https://doi.org/10.1016/j.eng.2019.12.011

Pan YH, 2021a. Miniaturized five fundamental issues about visual knowledge. *Front Inform Technol Electron Eng*, 22(5):615-618. https://doi.org/10.1631/FITEE.2040000

Pan YH, 2021b. On visual understanding. *Front Inform Technol Electron Eng*, early access. https://doi.org/10.1631/FITEE.2130000

Parajuli N, Lu A, Duncan JS, 2016. Left ventricle classification using active shape model and support vector machine. Proc 6$^{\text{th}}$ Int Workshop on Statistical Atlases and Computational Models of the Heart, p.154-161. https://doi.org/10.1007/978-3-319-28712-6_17

Rodero C, Strocchi M, Marciniak M, et al., 2021. Linking statistical shape models and simulated function in the healthy adult human heart. *PLoS Comput Biol*, 17(4):e1008851. https://doi.org/10.1371/journal.pcbi.1008851

Suinesiaputra A, Ablin P, Albà X, et al., 2018. Statistical shape modeling of the left ventricle: myocardial infarct classification challenge. *IEEE J Biomed Health Inform*, 22(2):503-515. https://doi.org/10.1109/JBHI.2017.2652449

Thermos S, Liu X, O'Neil A, et al., 2021. Controllable cardiac synthesis via disentangled anatomy arithmetic. Proc 24$^{\text{th}}$ Int Conf on Medical Image Computing and Computer-Assisted Intervention, p.160-170. https://doi.org/10.1007/978-3-030-87199-4_15

Van Dijck C, Wirix-Speetjens R, Jonkers I, et al., 2018. Statistical shape model-based prediction of tibiofemoral cartilage. *Comput Methods Biomech Biomed Eng*, 21(9):568-578. https://doi.org/10.1080/10255842.2018.1495711

Wolterink JM, Leiner T, Viergever MA, et al., 2018. Automatic segmentation and disease classification using cardiac cine MR images. Proc 8$^{\text{th}}$ Int Workshop on Statistical Atlases and Computational Models of the Heart, p.101-110. https://doi.org/10.1007/978-3-319-75541-0_11

Zheng Q, Delingette H, Ayache N, 2019. Explainable cardiac pathology classification on cine MRI with motion characterization by semi-supervised learning of apparent flow. *Med Imag Anal*, 56:80-95. https://doi.org/10.1016/j.media.2019.06.001

Zhou QY, Park J, Koltun V, 2016. Fast global registration. Proc 14$^{\text{th}}$ European Conf on Computer Vision, p.766-782. https://doi.org/10.1007/978-3-319-46475-6_47